nature communications

Article

https://doi.org/10.1038/s41467-025-64586-6

Structure and activation of the *Drosophila* insulin receptor by three *Drosophila* insulin-like peptides

Received: 3 January 2025

Accepted: 18 September 2025

Kai Cai[1,7], Michelle Ng[2,7], Rochele R. Yamamoto[3], Mohammed Akhter Hossain[4,5], Catherine Hall[2], John D. Wade[4,5], Marc Tatar[3] ✉, Eunhee Choi[2] ✉ & Xiao-chen Bai[1,6] ✉

Insulin/IGF signaling (IIS) is a highly conserved pathway essential for physiological regulation from yeast to mammals. In *Drosophila melanogaster*, a single insulin-like receptor (dmIR) interacts with various insulin-like peptides (DILPs), leading to diverse signaling and functional outcomes. However, the mechanisms by which different DILPs result in varied receptor activation and biological responses remain unclear. Here, we determine the cryo-electron microscopy (cryo-EM) structures of dmIR in complex with three DILPs: DILP1, DILP2, and DILP5. Our structural analyses reveal that each DILP induces distinct conformations of dmIR: the dmIR/DILP5 complex adopts the T-shaped asymmetric conformation with three bound DILP5 molecules; the dmIR/DILP2 complex displays the *Γ*-shaped asymmetric conformation with a single bound DILP2 molecule; and the dmIR/DILP1 complex shows both a *Γ*-shaped asymmetric conformation and a symmetric conformation that resembles a T-shape with a splayed stem. Functional assays demonstrate that the efficacy of DILP-mediated dmIR activation differs, with DILP5 inducing higher levels of receptor autophosphorylation, followed by DILP2 and DILP1. Together, these findings suggest that the distinct interactions between dmIR and DILPs dictate specific patterns of receptor activation.

Insulin/IGF signaling (IIS) is a fundamental pathway conserved from yeast to mammals. In vertebrates, three receptors have been identified within the insulin receptor (IR) family: IR, insulin-like growth factor 1 receptor (IGF1R), and insulin receptor-related receptor (IRR)[1–4]. These closely related receptors play critical roles in metabolic homeostasis, cell growth, development, and aging[5–8]. In contrast, invertebrates such as *Caenorhabditis elegans* (*C. elegans*) and *Drosophila melanogaster* (*Drosophila*) possess only one insulin-like receptor (Daf-2 in *C. elegans* and dmIR in *Drosophila*) that binds a variety of insulin-like peptides and consequently have extensive functional pleiotropy. The *C. elegans* genome encodes 40 insulin-like genes[9], whereas *Drosophila* encodes 7 insulin-like ligands (DILPs 1–7)[10,11]. The *Drosophila* IIS pathway regulates many physiological processes, including metabolism, growth, aging, reproduction, stress response, gut stem cell proliferation, innate immunity, and behavior[12–19]. It is a fundamental problem in both mammals and invertebrates to understand how such varied ligands interact with just a few receptors to differentially modulate so many phenotypes.

---

[1]Department of Biophysics, University of Texas Southwestern Medical Center, Dallas, TX, USA. [2]Department of Pathology and Cell Biology, Vagelos College of Physicians and Surgeons, Columbia University, New York, NY, USA. [3]Department of Ecology, Evolution and Organismal Biology, Brown University, Providence, RI, USA. [4]Florey Institute of Neuroscience and Mental Health, University of Melbourne, Melbourne, VIC, Australia. [5]School of Chemistry, University of Melbourne, Melbourne, VIC, Australia. [6]Department of Cell Biology, University of Texas Southwestern Medical Center, Dallas, TX, USA. [7]These authors contributed equally: Kai Cai, Michelle Ng. ✉e-mail: marc_tatar@brown.edu; EC3477@cumc.columbia.edu; Xiaochen.Bai@UTSouthwestern.edu

DmIR shares ~37% sequence identity with the mammalian IR and IGF1R[20]. Like IR and IGF1R, dmIR is assembled as a constitutive homodimer connected by disulfide bonds, with each protomer consisting of leucine-rich repeats (L1 and L2), a cysteine-rich region (CR), three fibronectin type III domains (FnIII-1, -2, -3), a carboxy-terminal tail of α-subunit (α-CT), transmembrane (TM), juxtamembrane (JM), tyrosine kinase (TK), and C-terminal (CT) domains (Supplementary Fig. 1a). However, there are key differences between dmIR and mammalian IR or IGF1R: dmIR has a much longer C-terminal tail (~480 residues longer) that contains binding sites for signaling molecules with SH2/SH3, PI3K and IRS (chico) domains that can trigger signaling cascades[21]. DmIR also contains an additional N-terminal domain (~340 residues) that is largely disordered and has unknown functions (Supplementary Fig. 1a). Furthermore, within the intracellular kinase insert domain (KID) of dmIR, dmIR contains a putative SH2 domain that is not found in the KID of mammalian receptors[12].

Recent cryo-EM analyses of mammalian IR and IGF1R[22–28] have provided many insights on how IIS ligands activate their receptors. At saturated insulin concentrations, four insulin molecules bind to two distinct sites on IR (denoted as site-1 and site-2), which transforms IR from the autoinhibited Λ-shaped (Λ is the Greek capital letter Lambda, or inverted V-shaped) conformation to a T-shaped symmetric conformation that renders full receptor activity. Site-1 involves the L1 and α-CT domains, while site-2 is located on the β-sheet of the FnIII-1 domain[24,26]. Under unsaturated insulin concentrations, IR adopts either *Γ*(Greek capital letter Gamma)- or Ƭ-shaped (Ƭ resembles letter T with a hook) asymmetric conformations with lower activity[23]. In contrast, IGF1R lacks site-2 binding, and due to the strong negative cooperativity between two site-1s, it only forms a *Γ*-shaped asymmetric conformation with a single IGF-1 bound[25]. Although IGF1R with symmetric conformation can form by disrupting the disulfide bridges between α-CTs, the symmetric IGF1R exhibits lower activity than the asymmetric IGF1R[25,29].

As the single insulin-like receptor of *Drosophila*, dmIR, together with its DILP ligands, modulates the range of functions controlled by mammalian IR and IGF1R. The pleiotropy of the *Drosophila* system may arise if various DILPs dictate specific signaling outcomes by uniquely influencing the conformation or stability of the dmIR active state[30]. This idea is consistent with observations where DILPs induce different kinetics of substrate phosphorylation, produce distinct transcriptional and phosphoproteomic profiles, and differentially control longevity[31–35]. Functional analysis of DILPs has been advanced by testing single peptides applied to cells. Post et al. studied the impact of both DILP2 and DILP5 peptides when applied to cultured *Drosophila* S2 cells[36]. DILP5 induces robust and sustained phosphorylation of Akt (pAkt), while DILP2 only stimulates an early spike of pAkt. On a broader scale, the transcriptional and protein phosphorylation profiles modulated by DILP2 and DILP5 overlap, yet these ligands also uniquely affect many outputs. For instance, DILP2 uniquely represses the phosphorylation of glycogen phosphorylase, while DILP5 increases the phosphorylation of sterile 20-like kinase and tramtrack[36]. Genetic analyses with adult *Drosophila* found that *dilp2* null mutants are longer-lived than WT *Drosophila*, whereas loss of *dilp5* alone has no impact on lifespan. Few functional data are available for other DILPs, and notably, adults do not typically express DILP1 except during overwintering diapause or when *dilp2* is knocked out[31,32], yet *dilp1* is required for the loss of *dilp2* to slow aging[32].

The way such distinct outcomes are produced may be clarified by structural studies of the interactions between DILPs with the dmIR. A recent cryo-EM study of the dmIR-ectodomain (ECD) bound to DILP5[37] revealed that the dmIR/DILP5 complex adopts a Ƭ-shaped asymmetric conformation, like that of the IR/insulin complex under unsaturated insulin concentrations[23]. Intriguingly, in that study, three DILP5 molecules are bound to dmIR, with two DILP5 molecules at site-1 and site-1′, and one at site-2. This arrangement is not observed in human or mouse IR/insulin complexes[22,24,25]. However, due to the lack of the structures of dmIR bound with different types of ligands, a comprehensive understanding of how different DILP ligands produce different receptor activation dynamics and biological functions remains unclear. To address this question, we pursued empirical structural and functional studies to uncover the relationships between ligand binding, conformational landscape of dmIR, and receptor activation and function.

In this work, we expressed and purified the near-full-length version of dmIR and determined its structures when bound with three different ligands—DILP1, DILP2, and DILP5, choosing these because they reflect a range of diverse phenotypic impacts[10,31,32,36]. All three DILP peptides are predicted to consist of two chains (A- and B-chains) connected by two disulfide bonds, similar to that of human insulin (Supplementary Fig. 1b). Cryo-EM analyses of dmIR/DILPs complexes reveal that the three DILPs induce distinct receptor conformations. The dmIR/DILP5 complex exhibits a Ƭ-shaped asymmetric conformation similar to that of dmIR-ECD/DILP5 structure, where three DILP5 molecules bind at site-1 (two DILP5 molecules) and at site-2 (one DILP5). The dmIR/DILP2 complex has a *Γ*-shaped asymmetric conformation where a single DILP2 binds the site-1 at the top region of the dmIR dimer. In contrast, the dmIR/DILP1 complex adopts two distinct conformations: a *Γ*-shaped asymmetric conformation like that of dmIR/DILP2 complex with one DILP1 molecule bound to the site-1, and a symmetric conformation with two DILP1 molecules bound to two site-1s. We further validate the structural observations using mutagenesis and cellular receptor activation assays. Our cell-based assays demonstrate that among the three DILP ligands, DILP5 induces higher levels of dmIR autophosphorylation, DILP2 is less effective than DILP5, and DILP1 shows the lowest efficacy in activating dmIR. Our results provide structural and functional evidence that the diverse insulin-like peptides in *Drosophila* induce distinct conformational interactions with a single insulin-like receptor, leading to varied receptor activation patterns and regulation of different cellular processes.

Results

Differential efficacy of DILP1, DILP2, and DILP5 in dmIR activation

To investigate the activation of dmIR by three synthetic ligands, DILP1, DIL2, and DILP5, we conducted cell-based assays using 293FT cells expressing dmIR and compared receptor activation across a range of ligand concentrations. We quantified dmIR autophosphorylation levels induced by DILP1 and DILP2 relative to those induced by DILP5 (Fig. 1a; Supplementary Fig. 2a).

DILP5 increased dmIR autophosphorylation in a dose-dependent manner, with saturation observed at 300 nM of DILP5 (Fig. 1a). In contrast, DILP2 increased dmIR autophosphorylation to approximately 75% of the efficacy achieved by DILP5 (Fig. 1a; efficacy is referred to as the signal in amplitude). DILP1 induced the lowest level of dmIR autophosphorylation (Fig. 1a), which was significantly lower than that induced by DILP2 and reached only about 50% of the DILP5 maximum. These results suggest that the different DILP peptides differentially activate dmIR.

Overall structure of dmIR bound with DILP1, DILP2, and DILP5

To understand the mechanism underlying the differential activation of dmIR induced by DILP1, DILP2, and DILP5, we carried out structural studies of dmIR in complex with the three ligands. A near-full-length dmIR (residues 1–50, 151–1675) was expressed using Sf9 cells and purified by affinity chromatography followed by size-exclusion chromatography. To improve protein expression yield, we introduced a kinase-dead mutation (D1519N) and two truncations: an N-terminal truncation (residues 50–150) and a C-terminal tail truncation (residues 1676–2143) (Supplementary Fig. 1c). DmIR/DILPs complexes were

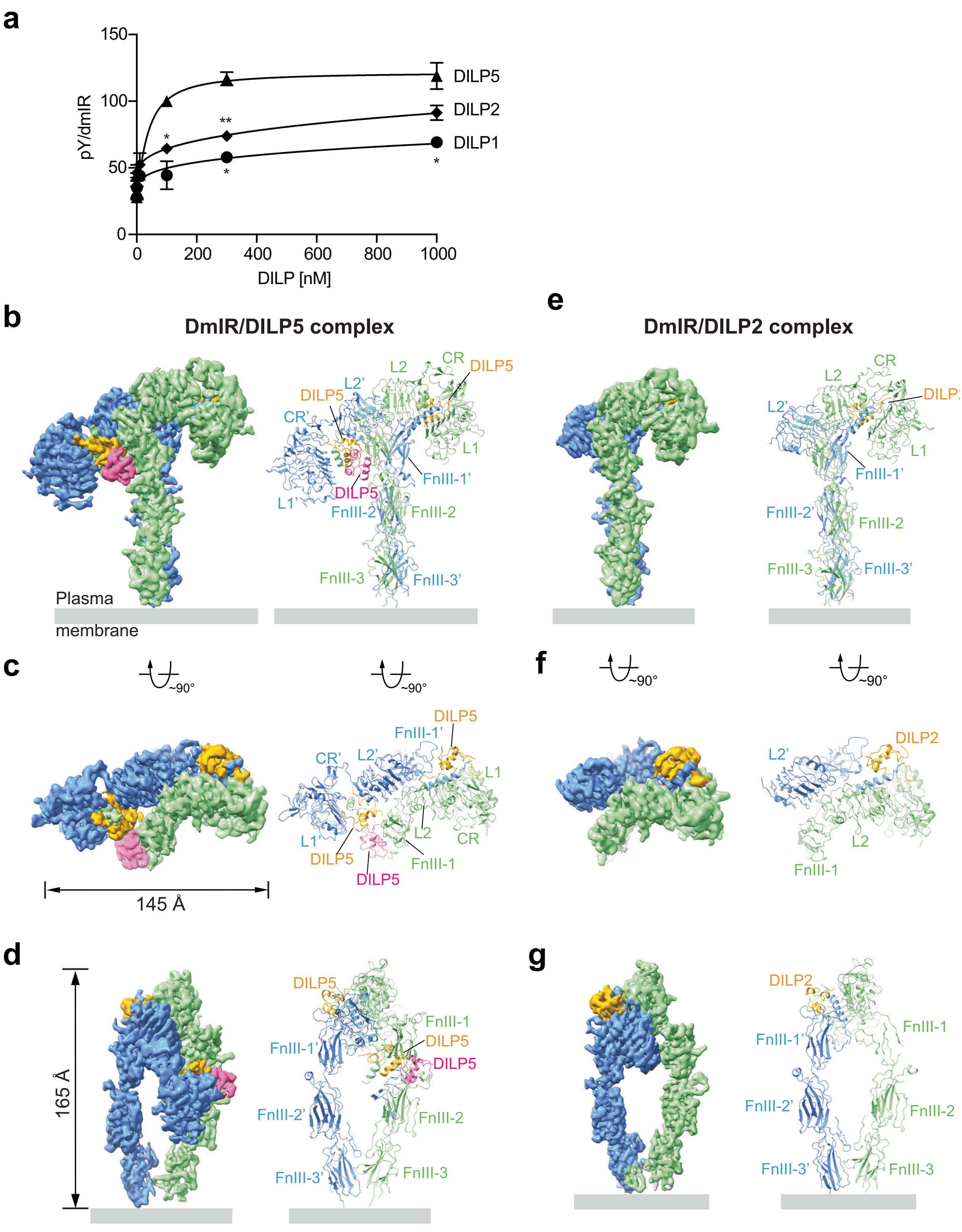

Fig. 1 | Overall structures of the dmIR/DILP5 and dmIR/DILP2 complexes. **a** Comparison of dmIR autophosphorylation at various concentrations of DILP1, DILP2, and DILP5. Cells expressing wild-type (WT) dmIR were treated with various concentrations of DILP1, DILP2, or DILP5 for 10 min. Mean ± SD. *N* = 3 for DILP1, DILP5; *N* = 4 for DILP2 (independent experiments). Statistical significances were determined using 2-way ANOVA. *P* values vs DILP5-treated WT dmIR. *$p < 0.05$, **$p < 0.01$. The exact p values are provided in the source data. Source data are provided as a Source data file. **b**–**d** 3D reconstructions and corresponding ribbon representations of dmIR/DILP5 complex are shown in three orthogonal views. Two protomers are shown in green and blue, DILP5 at site-1 is shown as yellow, and DILP5 at site-2 is shown as pink. **e**–**g** 3D reconstructions and corresponding ribbon representations of dmIR/DILP2 complex are shown in three orthogonal views. Two protomers are shown in green and blue, DILP2 at site-1 is shown as yellow.

Table 1 | List of residues on DILP1, DILP2 and DILP5 involved in binding dmIR

	Site-1	Site-1′	Site-2
DILP5	A3R, A5V, A6V, A7D, A11R, A21A, A22Y, A24D, B2S, B3L, B4R, B6C, B8P, B9A, B10L, B11M, B12D, B13M, B14L, B22F, B23N, B24S, B25M, B26F	A1D, A2F, A3R, A4G, A5V, A6V, A7D, A10C, A11R, A12N, A13S, A16F, A18T, A21A, A22Y, A23C, A24D, B1N, B6C, B8P, B10L, B11M, B15R, B22F, B23N, B23N, B24S, B25M, B26F	A16F, A20R, B1N, B3L, B11M, B12D, B13M, B15R, B16V, B17A, B19P
DILP2	A1Q, A3I, A4V, A5E, A9K, A14M, A19E, A20Y, A22S, B1T, B2L, B3C, B4S, B6K, B7L, B8N, B11L, B17E, B18Y, B19N, B20P, B21V, B22I, B23P		
DILP1 Symmetric	A6V, A7Y, A8D, A22I, A23Y, B16N, B17H, B18K, B20C, B21G, B22P, B23A, B24L, B25S, B26D, B28M, B29D, B34H, B36F, B37N, B38T, B39L, B40P	A6V, A7Y, A8D, A22I, A23Y, B16N, B17H, B18K, B20C, B21G, B22P, B23A, B24L, B25S, B26D, B28M, B29D, B34H, B36F, B37N, B38T, B39L, B40P	
DILP1 Asymmetric	A6V, A7Y, A8D, A22I, A23Y, B16N, B17H, B18K, B20C, B21G, B22P, B23A, B24L, B25S, B26D, B28M, B29D, B34H, B36F, B37N, B38T, B39L, B40P		

reconstituted in vitro by mixing dmIR and DILPs at a 1:4 molar ratio and subjected to cryo-EM analyses.

We determined the cryo-EM structures of near-full-length dmIR bound with DILP1, DILP2, or DILP5 (Supplementary Fig. 3). All of these cryo-EM structures were resolved at high quality (resolution of dmIR/DILP5: 3.6 Å; dmIR/DILP2: 3.7 Å; asymmetric dmIR/DILP1: 4.4 Å; symmetric dmIR/DILP1: 3.9 Å), allowing for accurate model building with the aid of domain structures predicted by AlphaFold2[38] (Supplementary Figs. 4–6). In all structures, the ECD of dmIR is well-resolved; however, the TM and kinase domains were not resolved in the cryo-EM maps due to high structural flexibility. DmIR bound with either DILP5 or DILP2 exhibited a single asymmetric conformation, with three and one ligands bound, respectively (Fig. 1b–g; Supplementary Figs. 4 and 5). In contrast, dmIR bound with DILP1 adopted two major conformations—asymmetric and symmetric (Supplementary Fig. 3c, d; Supplementary Fig. 6). Since the overall structure of our near-full-length dmIR bound with DILP5 closely resembles that of previously reported dmIR-ECD/DILP5 complex[37], we will not describe it in detail here. Instead, we will highlight the distinct structural features observed in the dmIR/DILP2 and dmIR/DILP1 complexes relative to the dmIR/DILP5 complex.

Structural comparison of site-1 in dmIR/DILP5 and dmIR/DILP2 complexes

The near-full-length dmIR bound with DILP5 exhibits a T-shaped asymmetric conformation (Fig. 1b–d; Supplementary Fig. 3a). In this T-shaped dmIR/DILP5 complex, three DILP5 molecules were observed: two DILP5 molecules bound at site-1 and site-1′, and one DILP5 molecule bound at site-2. A complete list of DILP5 residues involved in receptor binding is shown in Table 1 and Supplementary Fig. 7b.

The structure of dmIR/DILP2 complex exhibits an asymmetric conformation, with only one DILP2 molecule bound at site-1 in the top region of the dmIR (Figs. 1e–g and 2a, b; Supplementary Fig. 3b). One protomer of dmIR in dmIR/DILP2 complex closely resembles that of the dmIR/DILP5 complex. In the opposite protomer, while the L2, FnIII-1, FnIII-2, and FnIII-3 domains align well with those in the dmIR/DILP5 complex, the L1′ and CR′ domains are not resolved in the dmIR/DILP2 complex, likely due to the increased structural flexibility, unlike more stable configuration observed in the dmIR/DILP5 complex (Figs. 1 and 2c). The overall conformation of dmIR/DILP2 complex resembles a *Γ*-shape. To distinguish it from the previously described *Γ*-shaped asymmetric IR complex with one insulin molecule, or the IGF1R/IGF-1 complex, we refer to this configuration using an italicized gamma (*Γ*).

In addition, a subtle yet important distinction between the dmIR/DILP5 and dmIR/DILP2 complex structures lies in the relative orientation of the site-1 ligand-binding domains and the membrane-proximal domains (FnIII-1-3). Particularly, superimposition of the two structures using their site-1 ligand-binding domains (L1–CR–L2) reveals a displacement in the FnIII-2 and FnIII-3 domains (Fig. 2c). These conformational differences are likely caused by the binding of two additional DILP5 molecules in the central region of the receptor.

Table 2 | Activation of wild-type and mutants dmIR by DILP2 and DILP5

	DILP5 (%)[a]	DILP2 (%)[b]
WT	100	100
Site-1		
Q1040A	49.88 ± 6.204	62.34 ± 6.923
F1044A	47.81 ± 3.107	73.3 ± 6.97
R848A	30.54 ± 3.848	49.3 ± 2.803
R657A	77.82 ± 11.7	N.D.
Δ602–609	75.33 ± 4.766	N.D.
Site-2		
V889R	82.12 ± 2.988	N.D.
S820R	71.04 ± 5.726	N.D.
FnIII-3–FnIII-3 interaction		
D1251R	68.6 ± 6.589	54.09 ± 8.052
K1256A	70.01 ± 8.224	44.53 ± 7.604

N.D. not determined.

[a] Levels of dmIR autophosphorylation were normalized to total dmIR levels and are shown as intensities relative to that of dmIR-WT treated with 100 nM DILP5 for 10 min. Mean ± s.e.m.

[b] Levels of dmIR autophosphorylation were normalized to total dmIR levels and are shown as intensities relative to that of dmIR-WT treated with 100 nM DILP2 for 10 min. Mean ± s.e.m.

DILP2 and DILP5 bind to site-1 of dmIR in a similar fashion (Fig. 2a, b). In both structures, the ligands–DILP2 or DILP5–simultaneously interact with the L1/α-CT′-L2 domains (site-1a) and the FnIII-1′ domain (site-1b). Although DILP2 and DILP5 adopt similar binding modes at site-1, the sequence homology of the binding residues is relatively low. Of the 24 residues involved in site-1 binding by DILP2, only 6 are conserved in DILP5 (Supplementary Fig. 7b; Table 1). To confirm that DILP2 and DILP5 binding at site-1 are essential for dmIR activation in vivo, we introduced Q1040A and F1044A (site-1a) and R848A (site-1b) mutations into dmIR that were expressed in 293FT cells to disrupt this interface. DILP5 or DILP2 stimulation significantly increased autophosphorylation of dmIR WT in these human cells (Fig. 2f, g, blue bars; Supplementary Fig. 2b, c; Table 2), whereas the dmIR Q1040A, F1044A, and R848A mutants exhibited reduced receptor autophosphorylation, confirming the importance of site-1 interface for receptor activation.

In addition to the classical site-1 interface, DILP2 and DILP5 binding at site-1 has two unique characteristics. First, a loop in the CR domain of dmIR is longer than that in mammalian IR and folds into a β-hairpin structure (Fig. 2a, b; Supplementary Fig. 8a–c). This distinctive β-hairpin contacts both the α-CT′ motif and the bound ligands, further strengthening the interaction of ligands at site-1 (Fig. 2a, b). Second, the L1–CR–L2 domains of dmIR adopt a more compact

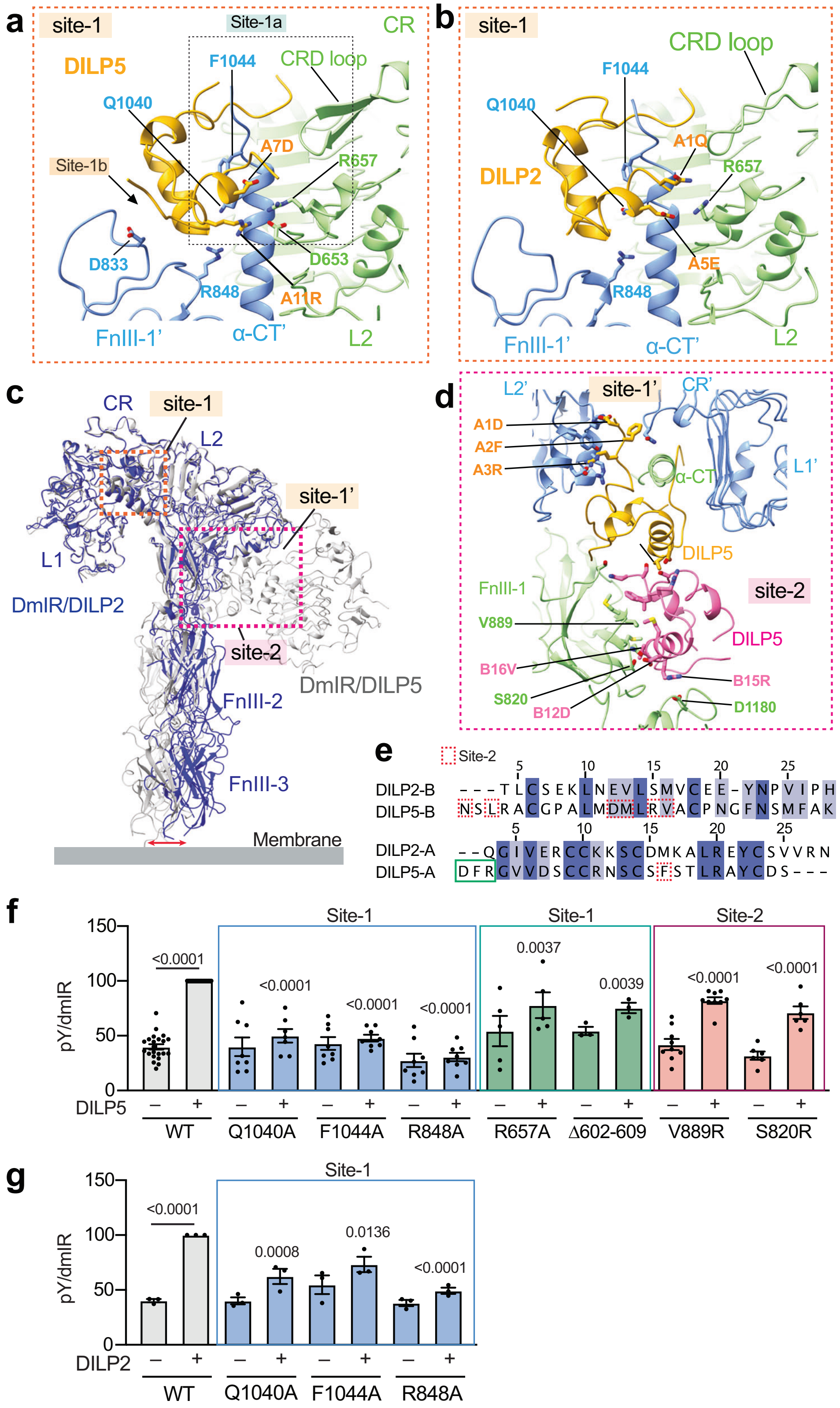

conformation in the top region of active dmIR compared to that of active mammalian IR (Supplementary Fig. 8a–c). As a result, the site-1-bound DILP2 or DILP5 can directly interact with the L2 domain (Fig. 2a, b). To validate the structural model, we introduced a truncation of residues 602–609 (CR domain, Δ602–609) and R657A mutation (L2 domain) into dmIR to disrupt these interfaces. DmIR Δ602–609 and R657A mutations led to impaired DILP5-induced activation of dmIR expressed in 239FT cells, supporting the important role of DIPL5/L1–CR–L2 domain interfaces in dmIR activation (Fig. 2f, green bars; Supplementary Fig. 2b; Table 2).

Compared with mammalian IR, dmIR has an additional N-terminal loop that inserts into the cleft between L1 and CR domains, stabilizing the L1–CR domains structure (Supplementary Fig. 8f). Indeed, mutations of this N-terminal loop (Δ328–338 and C339A) led to processing

Fig. 2 | Structural details of DILP2 and DILP5 binding to the active dmIR. Close-up view of the site-1 binding of DILP5 (**a**) and DILP2 (**b**) to dmIR. Site-1 DILP2 or DILP5 is shown in yellow, and two protomers of dmIR are shown in green and blue. **c** Structural comparison of dmIR/DILP5 and dmIR/DILP2 complexes. The structures of dmIR/DILP5 (gray) and dmIR/DILP2 (blue) are superimposed based on their site-1 ligand-binding site (L1–CR–L2 domains) and shown in ribbon representations. **d** Close-up view of the site-1′ and site-2 binding of DILP5 to dmIR. Site-1′ and site-2 DILP5 are shown in yellow and pink, respectively. Two protomers of dmIR are shown in green and blue. **e** Sequence alignment of the B- and A-chains of DILP2 and DILP5. Color code: dark blue, conserved residues; light blue, similar residues. The green box highlights the "DFR" motif on the N-terminus of A-chain of DILP5 that is important for the site-1′ binding, and the dotted red boxes highlight the DILP5 residues involved in site-2 binding to dmIR. **f** Autophosphorylation of dmIR in 293FT cells expressing dmIR wild-type (WT) or the indicated mutants. Cells were treated with 100 nM DILP5 for 10 min. Mean ± sem. N = at least 3 independent experiments. Statistical significance was determined using 2-way ANOVA. *P* values vs DILP5-treated dmIR WT. Exact *P* values are shown in the figure panel. **g** Autophosphorylation of dmIR in 293FT cells expressing dmIR wild-type (WT) or the indicated mutants. Cells were treated with 100 nM DILP2 for 10 min. Mean ± sem. *N* = 3 independent experiments. Statistical significance was determined using 2-way ANOVA. *P* values vs DILP2-treated dmIR WT. Exact *P* values are shown in the figure panel. Source data are provided as a Source data file.

defects (Supplementary Fig. 8g), indicating that the extended N-terminal loop of the L1 domain is essential for maintaining receptor structural integrity during processing.

Structural comparison of site-2 in dmIR/DILP5 and dmIR/DILP2 complexes

One key difference between the structures of dmIR/DILP5 and dmIR/DILP2 complexes is the presence of site-1′ and site-2 binding of DILP5 (Fig. 2c). The site-1′ DILP5 is located in the middle region of the T-shaped dmIR. Notably, the N-terminus of the A-chain of the site-1′ DILP5 (Asp-Phe-Arg, or "DFR" motif) inserts into a cleft formed between the CR′ and L2′ domains of dmIR, thereby stabilizing the relative orientation of these two domains (Fig. 2d). Site-2 DILP5 engages FnIII-1 domain of dmIR, similar to site-2 insulin binding observed in mammalian IR[23,24] (Fig.2d; Supplementary Fig. 7a; Table 1). Additionally, the site-2-bound DILP5 also makes direct contact with the site-1′-bound DILP5, and this DILP5–DILP5 interaction crosslinks the L1′/α-CT domains (site-1′) of one protomer with the FnIII-1 domain (site-2) of another protomer, thereby stabilizing the T-shaped asymmetric dmIR (Fig. 2d).

Analysis of the DILP5 residues involved in site-2 binding reveals that most of these key residues, such as B1N, B3L, B12D, B13M, B15R, and A16F, are not conserved in DILP2 (Fig. 2e), explaining why DILP2 does not bind to site-2 of dmIR. Moreover, the "DFR" motif, a key sequence at the N-terminus of the A-chain in DILP5 required for the site-1′ binding, is absent in DILP2 (Fig. 2e). This suggests that the N-terminus of site-1′-bound DILP2 cannot bridge and stabilize the CR′ and L2′ domains of dmIR, leading to the high flexibility of the L1′/α-CT–CR′ domains. Consistently, the L1′/α-CT–CR′ domains were not resolved in the cryo-EM map of the dmIR/DILP2 complex.

To validate the importance of site-2 binding, we introduced S820R and V889R mutations into dmIR to disrupt DILP5 binding at site-2. Both mutants exhibited a modest but statistically significant reduction in dmIR phosphorylation, supporting the role of site-2 binding in DILP5-induced dmIR activation (Fig. 2f, pink bars; Supplementary Fig. 2b; Table 2).

Receptor–receptor interactions in dmIR/DILP5 and dmIR/DILP2 complexes

The asymmetric conformation of dmIR in dmIR/DILP5 and dmIR/DILP2 complexes is stabilized by two key receptor–receptor interactions between the two protomers. First, the disulfide bond-linked long loops of the FnIII-1 domains (C873–C873′) adopt a rigid conformation in the asymmetric dmIR (Fig. 3a, b), contacting both the N-terminal portion of the α-CT′ motif and the L2′ domain. Second, in the membrane-proximal region, the side surfaces of the FnIII-3 domains (D1251-K1256′) also interact asymmetrically (Fig. 3c, d).

To validate the significance of this asymmetric receptor–receptor interaction in dmIR activation, we introduced D1251R and K1256A mutations into dmIR to disrupt the FnIII-3–FnIII-3′ interface. Both dmIR D1251R and K1256A mutants showed defects in DILP5- or DILP2-dependent dmIR activation, supporting our structural model (Fig. 3e, f; Supplementary Fig. 2b, c; Table 2).

These extensive ligand–receptor and asymmetric receptor–receptor interactions collectively stabilize the asymmetric conformation of dmIR and thus prevent the formation of the symmetric conformation of dmIR. In contrast, some of these asymmetric receptor–receptor interactions are absent in the mouse IR/insulin asymmetric complex (Supplementary Fig. 8a, b, d, e), which may in part explain why mammalian IR tends to form a T-shaped symmetric conformation at saturated ligand concentrations[23,24].

Structure of the dmIR/DILP1 complex

The dmIR bound with DILP1 adopts two major conformations: asymmetric and symmetric (Fig. 4; Supplementary Fig. 3c, d). The number of particles observed in each class is similar, indicating that DILP1 can induce both conformations with comparable capability. The asymmetric *Γ*-shaped conformation of dmIR bound with DILP1 closely resembles that of the dmIR/DILP2 complex, where only one ligand is bound at site-1 in the top region of the dmIR in a manner similar to DILP2 or DILP5 (Fig. 4a, b). Among the 23 DILP1 residues involved in site-1 binding, 11 are conserved with DILP5, and only 4 are conserved with DILP2 (Supplementary Fig. 7b; Table 1). Despite the high structural similarity (overall RMSD 0.47 Å), superposition of the two structures via the L1–CR–L2 domains reveals a displacement in the positioning of their FnIII-2 and FnIII-3 domains (Fig. 4b), akin to the shift observed in the dmIR/DILP5 versus dmIR/DILP2 comparison, albeit to a lesser extent (Fig. 2c).

In the symmetric dmIR/DILP1 complex, two DILP1 molecules are bound at site-1 and site-1′ in the top region of the dmIR, arranged with two-fold symmetry (Fig. 4c). Intriguingly, although the asymmetric conformations induced by DILP1 and DILP2 share high resemblance (Fig. 4b), only DILP1 can induce the symmetric conformation of dmIR. Structural comparison between the dmIR/DILP1, dmIR/DILP2, and dmIR/DILP5 complexes revealed that the extended N-terminal tail of DILP1 B-chain, including B16N, B17H, and B18K, makes additional interactions at site-1b (e.g., with D833 and D846 in the FnIII-1 domain of dmIR) (Fig. 5a–c; Supplementary Fig. 7b), which are not seen in dmIR/DILP2 complex. These stronger interactions at site-1b may shift the conformational equilibrium of dmIR from an asymmetric to a symmetric state, partly explaining why only DILP1 induces the symmetric conformation of dmIR. To test this hypothesis, we deleted the N-terminal residues "MVTPTGSGHQLLPPGNH" from the DILP1 B-chain (DILP1 ΔB1-17), which is likely responsible for promoting the asymmetric-to-symmetric conformational transition. Cell-based assays showed that DILP1 ΔB1-17 mutant exhibited a modest increase in activity compared to wild-type DILP1 (Supplementary Fig. 7c, d), supporting the role of the extended N-terminal tail of DILP1 B-chain in dmIR activation and suggesting that the symmetric conformation may be less active than the asymmetric conformation.

In addition, similar to DILP2, DILP1 lacks the extended "DFR" motif at the N-terminus of the A-chain found in DILP5, and key DILP5 resides

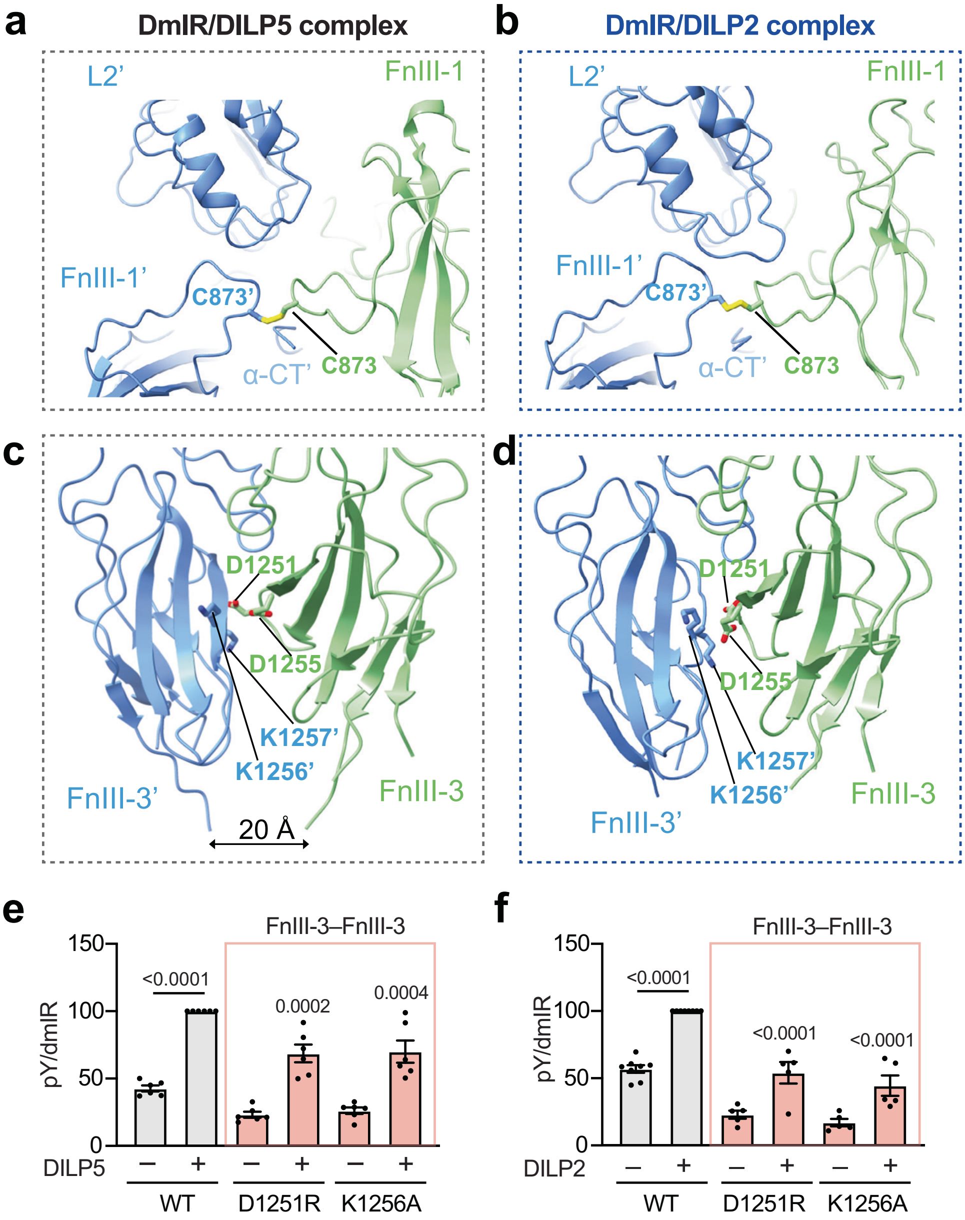

Fig. 3 | Domain-domain interactions in dmIR/DILP5 and dmIR/DILP2 complexes. a Close-up view of the tripartite interface formed by three loops from α-CT and FnIII-1 domains (green), FnIII-1′ and L2′ domains (blue) in DmIR/DILP5 complex. **b** Close-up view of the tripartite interface formed by three loops from α-CT and FnIII-1 domains (green), FnIII-1′ and L2′ domains (blue) in DmIR/DILP2 complexes. **c** Close-up view of the asymmetric interaction interface between FnIII-3-FnIII-3′ domains in DmIR/DILP5 complex. **d** Close-up view of the asymmetric interaction interface between FnIII-3-FnIII-3′ domains in DmIR/DILP2 complex. **e** Autophosphorylation of dmIR in 293FT cells expressing dmIR WT or the indicated mutants. Cells were treated with 100 nM DILP5 for 10 min. Mean ± sem. *N* = 6 independent experiments. Statistical significance was determined using 2-way ANOVA. *P* values vs DILP5-treated dmIR WT. Exact *P* values are shown in the figure panel. **f** Autophosphorylation of dmIR in 293FT cells expressing dmIR WT or the indicated mutants. Cells were treated with 100 nM DILP2 for 10 min. Mean ± sem. *N* = 5 independent experiments. Statistical significance was determined using 2-way ANOVA. *P* values vs DILP2-treated dmIR WT. Exact *P* values are shown in the figure panel. Source data are provided as a Source data file.

involved in site-2 binding are not conserved in DILP1 (Supplementary Fig. 7b). This explains why DILP1 also fails to bind at site-2 of dmIR.

The FnIII-3–FnIII-3′ interaction observed in the asymmetric dmIR/DILP1 complex is disrupted in the symmetric dmIR/DILP1 complex. Consequently, the two FnIII-3 domains no longer make contact and exhibit increased flexibility. This likely contributes to the lower-resolution cryo-EM density observed for the FnIII-3 domains in the symmetric complex compared to the asymmetric form (Fig. 4a, c, yellow boxes). Additionally, the distance between the last residues (P1305–P1305′) increases from about 20 Å in the asymmetric dmIR/DILP5 complex to about 28 Å in the symmetric DILP1/dmIR complex (Fig. 5d). The increased separation and flexibility of these membrane-proximal regions in the symmetric conformation suggest that this form is less active than the asymmetric one.

To test this possibility, we quantified the dmIR autophosphorylation levels following stimulation with either an excess amount of DILP1 or a combination of DILP1 and DILP5. Cells were treated with 1000 nM DILP1 alone, 100 nM DILP5 alone, or a combination of 1000 nM DILP1 and 100 nM DILP5 (Fig. 5f, g). Since DILP1 does not bind to site-2, we expected that DILP5 to occupy site-2 while both DILP1 and DILP5 could bind site-1, thereby stabilizing the asymmetric conformation. Consistent with our dose-response results (Fig. 1a), DILP1

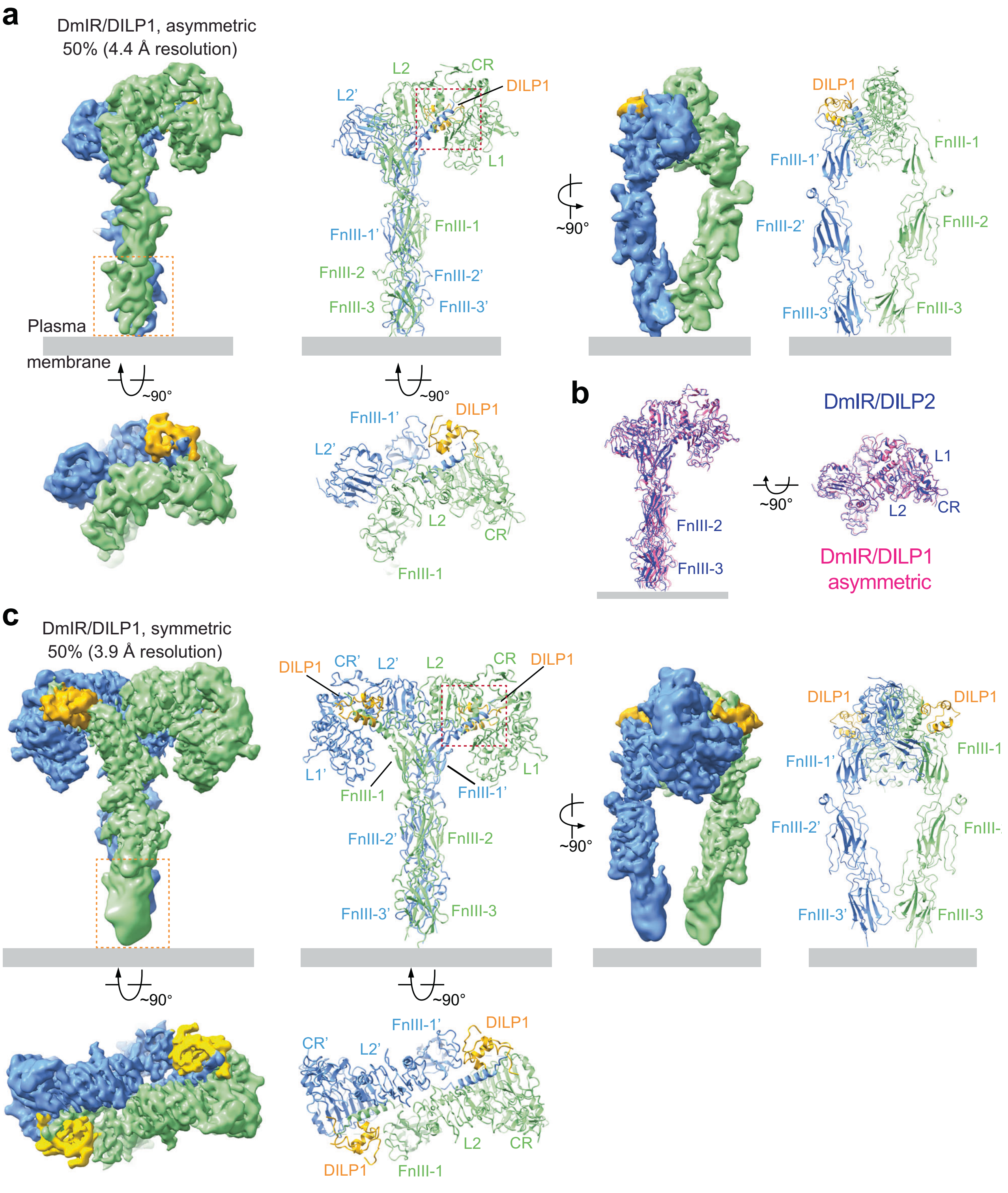

Fig. 4 | Overall structures of the dmIR/DILP1 complex. **a** Asymmetric conformation of dmIR/DILP1 complex. Two protomers are shown in green and blue. DILP1 is shown as yellow. 3D reconstructions and corresponding ribbon representations are shown in three orthogonal views. **b** Structural comparison of asymmetric dmIR/DILP1 and dmIR/DILP2. The ribbon representations of dmIR/DILP1 (pink) and dmIR/DILP2 (blue) overlayed onto each other shown in two orthogonal views. The two structures were aligned based on their site-1 ligand-binding site (L1–CR–L2 domains). **c** Symmetric conformation of dmIR/DILP1 complex. Two protomers are shown in green and blue. DILP1 molecules are shown as yellow. 3D reconstructions and corresponding ribbon representations are shown in three orthogonal views.

induced lower levels of dmIR autophosphorylation compared to DILP5, despite being used at a tenfold higher concentration. Notably, co-treatment with DILP1 and DILP5 induced robust dmIR autophosphorylation, comparable to that induced by DILP5 alone. This suggests that DILP5 binding at site-2 may prevent DILP1 from promoting the symmetric conformation of dmIR, thereby leading to higher level of receptor activation. These experiments provide indirect evidence to support the notion that the asymmetric conformation of

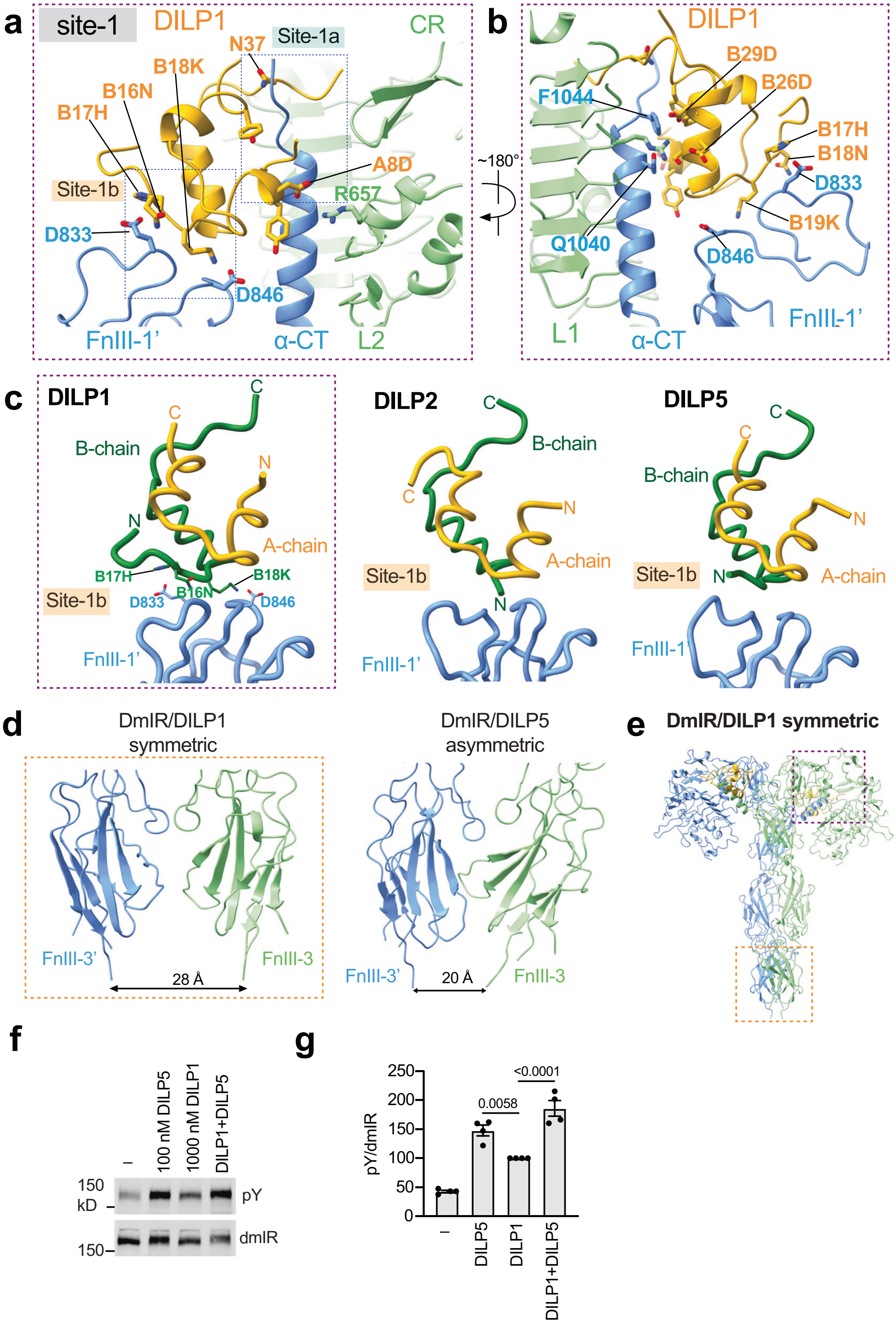

Fig. 5 | DILP1 binding site in symmetric dmIR and comparison of dmIR-ligand complexes. a, **b** Close-up view of the site-1 binding interface of DILP1 to dmIR shown in two views. **c** Comparison of site-1b binding sites of DILP1 (left), DILP2 (middle) and DILP5 (right) to the FnIII-1′ domain of dmIR. A-chains of DILP molecules are shown as yellow and B-chains as green. FnIII-1 domain of dmIR is shown in blue. **d** Comparison of FnIII-3 domains of DILP1-dmIR complex with symmetric conformation (left) and DILP5-dmIR complex (right). **e** Cartoon representation of dmIR/DILP1 complex with symmetric conformation. The two interfaces shown in panels a-d are indicated by dashed boxes with corresponding colors. Two protomers are shown in green and blue. Two DILP1 molecules are shown as yellow. **f** Representative images of DILP1- or DILP5-induced dmIR autophosphorylation in 293FT cells expressing dmIR wild-type. Cells were treated with 1000 nM DILP1, 100 nM DILP5, or a combination of 1000 nM DILP1 and 100 nM DILP5 for 10 min. Cell lysates were blotted with the indicated antibodies. **g** Quantification of the western blot data shown in (**f**). Mean ± sem. *N* = 4 independent experiments. Statistical significance was determined using 2-way ANOVA. Exact *P* values are shown in the figure panel. The exact p values are provided in the source data. Source data are provided as a Source data file.

dmIR is associated with higher receptor activity. Further structural and functional studies using ligand engineering to modulate the equilibrium between the asymmetric and symmetric conformations of dmIR are needed to fully define the relationship between receptor symmetry and activity.

Discussion

Our structural and functional analyses demonstrate that DILP1, DILP2, and DILP5 bind to dmIR in different ways, inducing unique active conformations of the receptor despite the high structural homology among the ligand peptides. Cell-based functional studies show that DILP5 elicits higher levels of dmIR autophosphorylation, followed by DILP2, while DILP1 induces the lowest dmIR autophosphorylation among the three ligands. These findings are consistent with previous observations in which DILP5 promotes robust and sustained pAKT signaling, whereas DILP2 triggers only transient pAKT spike[36].

Together, our results support the hypothesis that specific patterns of receptor–ligand interactions modulate the differential activity and signaling output of dmIR. Cryo-EM analysis reveals that dmIR adopts a single asymmetric conformation in the presence of excess DILP2 or DILP5. In the dmIR/DILP5 complex, three DILP5 molecules are observed: one is located at the top of the Ƭ-shaped dmIR, interacting with both the L1/α-CT′ (site-1a) and FnIII-1′ (site-1b) domains from opposing protomers (site-1). Two additional DILP5 molecules bind at site-1′ on one protomer and site-2 on the other, within the central region of the dmIR. These two DILP5 molecules directly interact with each other, collectively stabilizing the asymmetric conformation of the receptor. A similar Ƭ-shaped active conformation has been observed in mouse IR under subsaturating insulin conditions (Supplementary Fig. 8). However, in the Ƭ-shaped mouse IR, a single insulin molecule simultaneously contacts both site-1′ and site-2[22,23].

In addition to ligand–receptor interactions, the asymmetric Ƭ-shape of dmIR is reinforced by extensive asymmetric receptor–receptor interactions, including disulfide-linked loops within the FnIII-1 domains and direct contacts between two FnIII-3 domains. These combined ligand–receptor and receptor–receptor interactions stabilize the asymmetric dmIR conformation and may restrict the formation of a symmetric state.

In contrast to DILP5, only one DILP2 (site-1) is observed in the dmIR/DILP2 complex, which shares the similar binding environment as the site-1 DILP5 in dmIR/DILP5 complex. While we cannot rule out the possibility of binding of a second DILP2 molecule at site-1′ of dmIR, the pronounced structural flexibility of the L1–CR domains in this region prevents us from building a model reliably. Despite this difference in ligand occupancy, DILP2 induces an asymmetric conformation that closely resembles the conformation stabilized by three DILP5 molecules bound at both site-1 and site-2. Therefore, the precise functional role of DILP5 binding at site-2 remains unclear. Likewise, the molecular basis for DILP5's higher activity compared to DILP2 is not fully understood. One possibility is that the asymmetric dmIR conformation induced by DILP5 is more stable than that induced by DILP2, potentially due to additional receptor–ligand interactions. This increased stability may enhance membrane retention and, consequently, lead to greater receptor activation. However, this hypothesis has not yet been experimentally validated. Beyond conformational stability, other factors—such as the biochemical properties of the ligands, their potential for self-association, or differences in receptor binding kinetics—may also contribute to their distinct functional profiles. To resolve these possibilities and clarify the role of site-2 binding, further structural, biochemical, and mutagenesis studies combined with ligand engineering will be required.

In contrast to both DILP5 and DILP2, DILP1 induces both asymmetric and symmetric dmIR conformations. Like DILP2, DILP1 does not bind to dmIR site-2. However, it appears to engage more strongly at site-1b, likely due to an extended N-terminal region on its B-chain. This enhanced interaction at site-1b may facilitate the conformational transition from an asymmetric to a symmetric state. Our cell-based assays show that DILP1 has lower activity in activating dmIR compared to DILP2 and DILP5, suggesting that the symmetric conformation is less active. Consistent with this, the FnIII-3 domains of the symmetric dmIR/DILP1 complex exhibit increased flexibility and a greater distance between the membrane-proximal domains (~28 Å) compared to the ~20 Å observed in the asymmetric complex.

In wild-type *Drosophila*, DILP1 is only expressed during pupal stages or during overwinter diapause where adults are long-lived, experience low metabolic rate and have limited nutrients[31,39,40]. We postulate that a low-activating insulin-like hormonal peptide such as DILP1 may favor survival under these conditions. Notably, the longevity of non-diapause adults can be extended by knockout of *dilp2*, which leads to increased *dilp1* expression. Genetic epistasis analysis shows that *dilp1* is required for extended survival of *dilp2* mutants[32]. Tatar has proposed that the degree of receptor stability induced by each insulin-like peptides dictates the extent and quality of receptor and substrate phosphorylation, that in turn induces unique phenotype sets corresponding to specific insulin-like peptides[30]. The distinct structural interactions of DILP1 and DILP2 with dmIR observed in our study are consistent with this model.

Mammalian IR and IGF1R have distinct ligand preferences, ligand occupancy, and active conformations, despite their high structural similarity[22]. The conformation and activity of IR are modulated by the number of bound insulin molecules: one to three insulin molecules induce an asymmetric conformation with lower activity, whereas four insulin molecules drive the formation of a symmetric, high-activity conformation[23]. In contrast, IGF1R binds only one IGF-1 molecule due to a strong negative cooperativity between site-1s and instability at site-2[25]. A mutant IGF1R with increased α-CT flexibility can bind two IGF-1 molecules and adopt a symmetric conformation; however, this symmetric IGF1R is less active than the asymmetric IGF1R[23,29]. These findings suggest that dmIR behaves more like mammalian IGF1R rather than mammalian IR—it displays relatively higher activity in response to ligands (DILP2 or DILP5) that induce only asymmetric conformations, and lower activity in response to a ligand (DILP1), which induces both asymmetric and symmetric conformations (Fig. 6). Altogether, this unique system allows dmIR to adopt diverse conformations and activity profiles depending on ligand type and physiological context.

During structure determination, receptor–ligand complexes were prepared at a 1:4 molar ratio, raising the question of whether these conditions reflect maximal ligand saturation, and what structural changes might occur under very high ligand concentrations. In the DILP5/dmIR complex, one protomer exhibits canonical site-2 binding via its FnIII-1 domain, while the corresponding FnIII-1 domain on the opposing protomer remains unoccupied. This asymmetry suggests that the binding of the second site-2 DILP5 (site-2′) is either inherently weak in the absence of a stabilizing site-1′ interaction, or is negatively regulated by inter-site cooperativity between site-1 and site-2′. Under conditions of very high ligand concentration, it is conceivable that the second site-2 DILP5 could engage the vacant FnIII-1 domain, resulting in a fully ligand-occupied (4-ligand-bound) complex. Alternatively, the engagement of the second site-2 ligand may trigger a conformational rearrangement, yielding a symmetric, fully saturated receptor conformation—resembling the human IR/insulin complex under ligand-saturated conditions. A similar mechanism may also apply to other DILP ligands. For instance, in the DILP2/dmIR complex, only one DILP2 is bound between site-1a and site-1b′ on the top part of the asymmetric receptor. Under very high ligand conditions, however, it is plausible that both site-1 and sites-2 could be occupied by DILP2, leading to

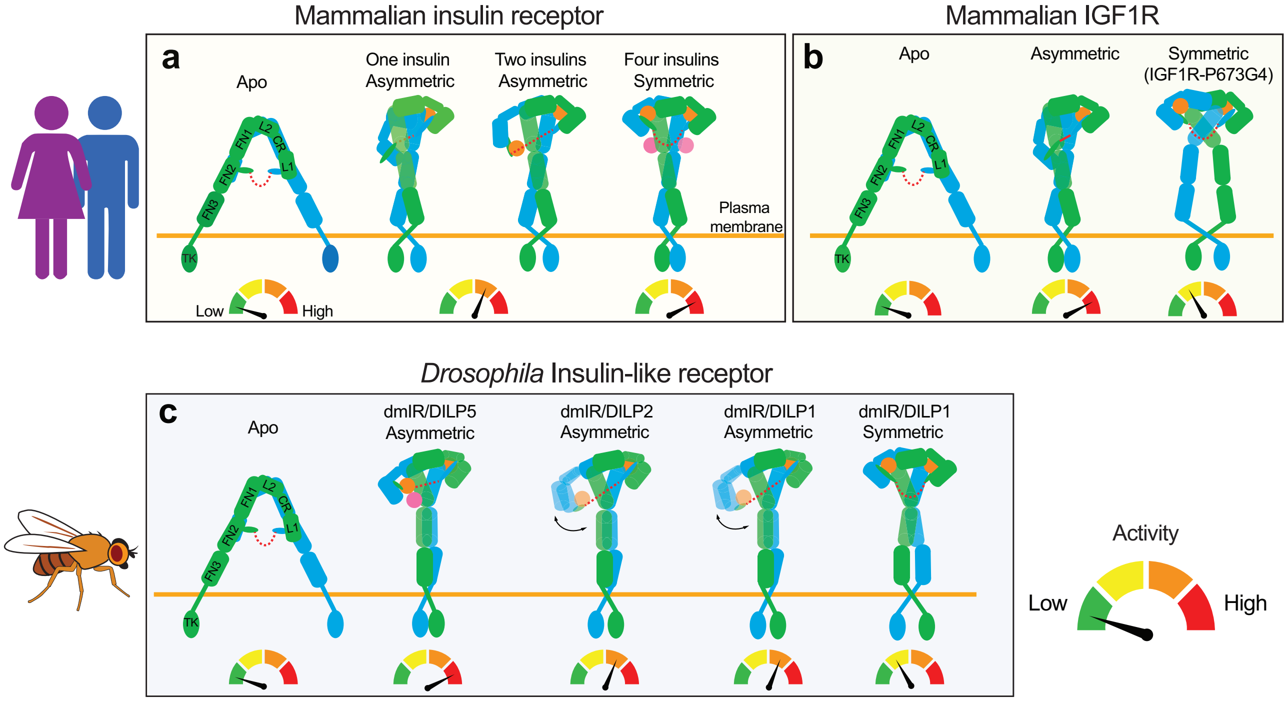

Fig. 6 | Proposed receptor activation models: dmIR, IR, and IGF1R. a Insulin-induced IR activation at various insulin concentrations. Under unsaturated insulin conditions, IR adopts an *Γ*-shaped asymmetric conformation with one insulin bound or T-shaped asymmetric conformation with two insulins bound, both of which may exhibit partial receptor activity. Under saturated insulin conditions, IR adopts a T-shaped symmetric conformation with four insulins molecules bound, resulting in full receptor activity. **b** IGF-1 induced IGF1R activation. The *Γ*-shaped asymmetric conformation of IGF1R with only one IGF-1 bound has the full receptor activity, whereas the T-shaped symmetric conformation of IGF1R-P674G4 with two IGF-1 molecules bound shows lower receptor activity. **c** DmIR activation induced by DILP1, DILP2, or DILP5. DILP2 and DILP5 induce only asymmetric conformations of dmIR. DILP5 binding at site-2 stabilizes the asymmetric dmIR conformation and enhances receptor activation. DILP2, which lacks site-2 interaction and has a shorter A-chain N-terminus, forms a less stable asymmetric conformation and activates dmIR less potently than DILP5. In contrast, DILP1 induces both asymmetric and symmetric conformations of dmIR. The symmetric dmIR conformation shows lower receptor activity relative to the asymmetric form, likely due to the increased distance between the two membrane-proximal regions.

increased ligand occupancy and possibly symmetric receptor conformations (Supplementary Fig. 9).

Although our studies provide key insights into the differential activation of dmIR by DILP1, DILP2 and DILP5, several limitations remain. First, while the three DILP ligands share similar overall structures, their sequence homology is relatively low. For example, despite the conserved architecture of site-1 binding, only six residues are conserved between DILP2 and DILP5, and only four between DILP1 and DILP2. The contributions of these sequence differences to receptor activation remain unclear. Second, although we used near-full-length dmIR for cryo-EM studies, the intracellular regions could not be modeled due to high structural flexibility. To facilitate protein purification, we also removed the extended N-terminus of the extracellular domain. How *Drosophila*-specific structural elements—including the extended N-terminal region of the ectodomain, the intracellular kinase insert domain, and the longer C-terminal tail—contribute to ligand-specific receptor activation is an important question for future investigation. Third, our functional assays were performed in mammalian cells, which represent a non-native, heterologous system. Future studies using *Drosophila* cells or in vivo models will be more appropriate to assess the physiological relevance of these findings. Finally, we examined phosphorylation only at the kinase domain site Y1548/1549 of dmIR. How other phosphorylation sites respond to different DILPs—and how these autophosphorylation patterns related to downstream signaling and physiological outcomes in *Drosophila*—remains to be determined. Future studies are needed to address these questions and to fully elucidate the molecular mechanisms by which distinct DILPs regulate dmIR signaling and function.

Methods

Protein expression and purification

For structural studies, the near-full-length dmIR was cloned into pFastBac expression vector. To improve the protein expression yield, a kinase-dead mutation D1519N and two truncations: a N-terminal truncation (residues 50–150) and a C-terminal tail truncation (residues 1676–2143) were introduced (Supplementary Fig. 1c). The Human Rhinovirus 3 C recognition site (3 C), affinity purification tag Tsi3 (T6SS secreted immunity protein three from Pseudomonas aeruginosa) and His8 tag were fused to the C-terminus of proteins. The plasmid was transformed to *Escherichia coli* strain DH10Bac to produce bacmid DNA. Recombinant baculovirus was generated by transfecting Sf9 cells with bacmid DNA using Cellfectin reagent (Gibco). DmIR was expressed in Sf9 cells by infecting the cells with the virus at 1:50 (virus: cell, v/v) ratio. Cells were cultured in a shaking incubator for 72 h at 24 °C before harvesting.

The cells were resuspended in lysis buffer containing 40 mM Tris-HCl pH 7.5, 400 mM NaCl (Buffer A) and Protease Inhibitor Cocktail (Roche) and lysed by using a French Press cell disruptor. The membrane fraction was obtained by ultracentrifugation of the cell lysate for 1 h at 100,000 × *g* at 4 °C. To extract the protein from the membrane fraction, Dodecyl maltoside (DDM, Anatrace) was added to a final concentration of 1% with stirring overnight. The supernatant containing the solubilized dmIR protein was obtained by ultracentrifugation for 1 h at 100,000 × *g* at 4 °C. The supernatant was added with 2 mM $CaCl_2$ and Tse3 protein-conjugated Sepharose resin (GE Healthcare) and incubated at 4 °C for 1 h before being loaded onto a column by gravity flow. The resin was subsequently washed with 40 column volume (CV) of buffer containing 40 mM Tris-HCl pH 7.5, 400 mM

Table 3 | Cryo-EM data collection and refinement statistics

	DmIR/DILP5	DmIR/DILP2	DmIR/DILP1 (Asymmetric)	DmIR/DILP1 (Symmetric)
Data collection and processing				
Magnification	105,000	105,000	105,000	105,000
Voltage (kV)	300	300	300	300
Electron exposure (e^{-}/Å^{2})	50	50	50	50
Defocus range (μm)	−0.8 to −2.2	−0.8 to −2.2	−0.8 to −2.2	−0.8 to −2.2
Pixel size (Å)	1.1	1.1	1.1	1.1
Symmetry imposed	C1	C1	C1	C2
Initial particle images (no.)	5,277,677	3,557,580	2,094,871	2,094,871
Final particle images (no.)	49,602	50,277	23,556	25,580
Map resolution (Å)	3.6	3.7	4.4	3.9
FSC threshold	0.143	0.143	0.143	0.143
Refinement				
Model composition				
Nonhydrogen atoms	14,853	11,505	11,404	14,493
Protein residues	1851	1421	1418	1806
Ligands	NAG	NAG	NAG	NAG
R.m.s. deviations				
Bond lengths (Å)	0.004	0.003	0.003	0.003
Bond angles (°)	0.626	0.632	0.667	0.647
Validation				
MolProbity score	1.93	1.93	2.00	1.98
Clashscore	7.30	7.42	8.34	8.39
Poor rotamers (%)	0.36	0.31	0	0.62
Ramachandran plot				
Favored (%)	90.87	91.05	89.87	90.64
Allowed (%)	8.74	8.52	9.48	8.91
Disallowed (%)	0.38	0.43	0.65	0.45

NaCl, 2 mM $CaCl_2$, 5% glycerol and 0.05% DDM (Buffer B) and eluted by HRV-3 C protease cleavage at 4 °C overnight. The protein was then concentrated using a 100 kDa cutoff concentrator (Millipore), loaded onto a Superose 6 increase 10/300 GL size-exclusion column (Cytiva), and eluted with buffer containing 20 mM HEPES pH 7.4, 150 mM NaCl and 0.03% DDM (Buffer C). The dimer fractions of dmIR protein were identified by SDS-PAGE and pooled (Supplementary Fig. 1d, e).

To make dmIR/DILP1, dmIR/DILP2 and dmIR/DILP5 complexes for cryo-EM analyses, the DILP ligands were added to dmIR at a molar ratio of 4:1 (DILPs:dmIR). After incubation for 30 min, the protein mixtures were concentrated to 6–8 mg ml^{-1} using 100 kDa cutoff concentrators (Millipore). After concentrating the protein complexes to desired concentrations, two additional molar equivalents of DILP peptides were added to the final sample. The protein samples were subject to cryo-EM grid preparation immediately. All purification and following steps were performed at 4 °C or on ice.

Cryo-EM data collection and image processing

EM data acquisition, image processing, model building, and refinement were performed following previous protocols with some modifications. The samples of dmIR in complex with DILP1, DILP2, or DILP5 were applied to glow-discharged Quantifoil R1.2/1.3 300-mesh gold holey carbon grids (Quantifoil, Micro Tools GmbH, Germany). Grids were blotted under 100% humidity at 4 °C and plunge-frozen in liquid ethane using a Mark IV Vitrobot (Thermo Fisher Scientific). Micrographs were collected in the counting mode on Titan Krios microscopes (Thermo Fisher Scientific) with K3 Summit direct electron detectors (Gatan). The nominal magnification and pixel size of each data set are summarized in Table 3. Motion-correction and dose-weighting of the micrographs were carried out using the Motioncor2 program (version 1.2)[41]. GCTF 1.06 was used for CTF correction[42]. Template-based particle picking was carried out using the autopick tool in RELION 5.0[43]. Particles were cleaned up with multiple rounds of 2D and 3D classification in RELION. Good particles were selected and subjected to 3D refinement. We cannot rule out the possibility that some transient conformations of dmIR, which might be potentially functionally important, were not captured in the cryo-EM analysis due to their conformational flexibility and low particle abundance. The exact procedures are summarized in supplementary figures. The initial mode for 3D classification and refinement was generated using the SGD method in RELION. The refined maps were further improved by using Bayesian polishing, blush regularization, and CTF refinement at the final stage. The Fourier Shell Correlation (FSC) 0.143 criterion was used for estimating the resolution of the maps. Local resolution was calculated in RELION.

Model building and refinement

The initial models of DILP5, DILP2, DILP1 and each domain of dmIR are generated by AlphaFold2[38]. Models building of dmIR/DILP5, dmIR/DILP2, dmIR/DILP1 symmetric and asymmetric complexes was initiated by rigid-body docking of each individual domain of dmIR and the ligands into the respective density maps using UCSF ChimeraX[44]. These initial models were manually modified using program Coot 1.1[45] and refined by using the real-space refinement module in the Phenix package (V1.20)[46]. Restraints on secondary structure, backbone Ramachandran angels, residue sidechain rotamers were used during the refinement to improve the geometry of the model. For the model building of N-glycans, the models of N-glycans (NAGs) were generated by Coot 1.1 and docked into the cryo-EM density as initial models, followed by another round of real-space refinement by using Phenix. A final round of refinement was performed using ISOLDE[47]. The final refined models were validated by MolProbity program[48] in the Phenix package (Table 3). Figures of the cryo-EM structures and density maps were generated using USCF ChimeraX.

Peptide synthesis

Wild-type DILP1, DILP2 and DILP5 were synthesized as reported previously[49]. Briefly, A- and B-chains were separately assembled by optimized Fmoc-solid phase peptide synthesis. Orthogonal cysteine S-protection was employed to enable subsequent sequential formation of the three disulfide bonds following liberation of the chains from the solid support by trifluoroacetic acid. After a final RP-HPLC purification, the synthetic DILP1 and DILP2 were comprehensively chemically characterized including by MALDI-TOF mass spectrometry and the net peptide content determined by amino acid analysis. DILP1 with B-chain N-terminus truncation (MVTPTGSGHQLLPPGNH, ΔB1-17) were purchased from Phoenix Pharmaceuticals Inc.

Cell lines

293FT. 293FT cells (R70007, Invitrogen) and IR and IGF1R double knockout 293FT cells[50] were cultured in high-glucose (4.5 g/L) DMEM supplemented with 10% (v/v) FBS, 2 mM L-glutamine, and 1% penicillin/streptomycin. Cells were maintained at 37 °C with a humidified atmosphere of 5% CO_2.

Cell-based insulin receptor activation assay

The dmIR activation assay was performed as previously described with some modifications[24,25,50,51]. A cDNA of full-length dmIR (wDah wild-type, GenBank Accession MT_563159) was cloned into the pCS2 vector[52] with a MYC tag at the C-terminus of dmIR. In order to validate our dmIR structures, we generated dmIR mutants designed to disrupt proposed binding interfaces using Q5 site-directed mutagenesis kit (New England Biolabs). Plasmid transfection in cells was performed with Lipofectamine 2000 (Invitrogen). After 1 day, the cells were serum-starved for 16–18 h. Serum-starved cells were treated with the indicated concentrations of DILP1, DILP2, or DILP5 for 10 min. There is no difference in potency between Phoenix Pharmaceuticals peptides and in-house peptides. After treatment, cells were incubated with cell lysis buffer [50 mM Hepes pH 7.4, 150 mM NaCl, 10% (v/v) Glycerol, 1% (v/v) Triton X-100, 1 mM EDTA, 10 mM sodium fluoride, 2 mM sodium orthovanadate, 10 mM sodium pyrophosphate, 0.5 mM dithiothreitol (DTT), 2 mM phenylmethylsulfonyl fluoride (PMSF)] supplemented with cOmplete Protease Inhibitor Cocktail (Roche) and PhosSTOP (Roche) on ice for 1 h. After centrifugation at 18,213 × g at 4 °C for 20 min, cell lysates were analyzed by SDS-PAGE and Western blotting. Anti-IR-pY1150/1151 (1:2000, 19H7, Cell signaling; pY1548/1549 for dmIR, labeled as pY) and anti-Myc (1:1000; 9E10, Roche; labeled as dmIR) were used as primary antibodies. For quantitative Western blots, anti-rabbit immunoglobulin G (IgG) (H+L) (Dylight 800 conjugates) and anti-mouse IgG (H+L) (Dylight 680 conjugates) (Cell signaling) were used as secondary antibodies. The membranes were scanned with the Odyssey Infrared Imaging System (LI-COR, Lincoln, NE). Levels of pY-dmIR were normalized to total dmIR levels and shown as intensities relative to that of dmIR-WT treated with 100 nM DILP2, 100 nM DILP5 or 1000 nM DILP1 for 10 min. We note that although 293FT cells express endogenous human IR, the size difference between dmIR and hIR is ~80 kDa and therefore the signal from hIR can be easily separated by SDS-PAGE. Quantification of the phosphorylated band of dmIR should therefore only include the expressed dmIR in all cases despite being expressed in human cells.

Statistical analysis

Prism 10 was used for the generation of graphs and for statistical analyses. Results are presented as mean ± SD or mean ± sem. Two-way ANOVA followed by the Dunnett test was used for multiple comparisons. Power analysis for sample sizes was not performed. Randomization and blinding methods were not used, and data were analyzed after the completion of all data collection in each experiment.

Reporting summary

Further information on research design is available in the Nature Portfolio Reporting Summary linked to this article.

Data availability

All reagents generated in this study are available with a completed Materials Transfer Agreement. All cryo-EM maps and models reported in this work has been deposited into EMDB/PDB database, under the entry ID: EMD-47967 (dmIR/DILP1, asymmetric conformation) [https://www.ebi.ac.uk/emdb/EMD-47967], 9EF1(dmIR/DILP1, asymmetric conformation), EMD-47969 (dmIR/DILP1, symmetric conformation) [https://www.ebi.ac.uk/emdb/EMD-47969], 9EF4 (dmIR/DILP1, symmetric conformation), EMD-47970 (dmIR/DILP2) [https://www.ebi.ac.uk/emdb/EMD-47970], 9EF5 (dmIR/DILP2), EMD-47971 (dmIR/DILP5) [https://www.ebi.ac.uk/emdb/EMD-47971], 9EF9 (dmIR/DILP5). Source data are provided with this paper.

References

1. Ullrich, A. et al. Human insulin receptor and its relationship to the tyrosine kinase family of oncogenes. *Nature* **313**, 756–761 (1985).
2. Ebina, Y. et al. The human insulin receptor cDNA: the structural basis for hormone-activated transmembrane signalling. *Cell* **40**, 747–758 (1985).
3. Shier, P. & Watt, V. M. Primary structure of a putative receptor for a ligand of the insulin family. *J. Biol. Chem.* **264**, 14605–14608 (1989).
4. Ullrich, A. et al. Insulin-like growth factor I receptor primary structure: comparison with insulin receptor suggests structural determinants that define functional specificity. *EMBO J.* **5**, 2503–2512 (1986).
5. Haeusler, R. A., McGraw, T. E. & Accili, D. Biochemical and cellular properties of insulin receptor signalling. *Nat. Rev. Mol. Cell Biol.* **19**, 31–44 (2018).
6. Mathew, R., Pal Bhadra, M. & Bhadra, U. Insulin/insulin-like growth factor-1 signalling (IIS) based regulation of lifespan across species. *Biogerontology* **18**, 35–53 (2017).
7. Yakar, S., Wu, Y., Setser, J. & Rosen, C. J. The role of circulating IGF-I: lessons from human and animal models. *Endocrine* **19**, 239–248 (2002).
8. Forbes, K. & Westwood, M. The IGF axis and placental function. A mini review. *Horm. Res* **69**, 129–137 (2008).
9. Zheng, S. et al. A functional study of all 40 Caenorhabditis elegans insulin-like peptides. *J. Biol. Chem.* **293**, 16912–16922 (2018).
10. Gronke, S., Clarke, D. F., Broughton, S., Andrews, T. D. & Partridge, L. Molecular evolution and functional characterization of Drosophila insulin-like peptides. *PLoS Genet.* **6**, e1000857 (2010).
11. Wu, Q. & Brown, M. R. Signaling and function of insulin-like peptides in insects. *Annu. Rev. Entomol.* **51**, 1–24 (2006).
12. Yamamoto, R., Palmer, M., Koski, H., Curtis-Joseph, N. & Tatar, M. Aging modulated by the Drosophila insulin receptor through distinct structure-defined mechanisms. *Genetics* **217**, https://doi.org/10.1093/genetics/iyaa037 (2021).
13. Lin, X. & Smagghe, G. Roles of the insulin signaling pathway in insect development and organ growth. *Peptides* **122**, 169923 (2019).
14. Miguel-Aliaga, I., Jasper, H. & Lemaitre, B. Anatomy and physiology of the digestive tract of Drosophila melanogaster. *Genetics* **210**, 357–396 (2018).
15. Gruntenko, N. E. & Rauschenbach, I. Y. The role of insulin signalling in the endocrine stress response in Drosophila melanogaster: a mini-review. *Gen. Comp. Endocrinol.* **258**, 134–139 (2018).
16. Teleman, A. A. Molecular mechanisms of metabolic regulation by insulin in Drosophila. *Biochem J.* **425**, 13–26 (2009).

17. Weger, A. A. & Rittschof, C. C. The diverse roles of insulin signaling in insect behavior. *Front. Insect. Sci.* **4**, 1360320 (2024).
18. Das, D. & Arur, S. Conserved insulin signaling in the regulation of oocyte growth, development, and maturation. *Mol. Reprod. Dev.* **84**, 444–459 (2017).
19. Darby, A. M. & Lazzaro, B. P. Interactions between innate immunity and insulin signaling affect resistance to infection in insects. *Front. Immunol.* **14**, 1276357 (2023).
20. Fernandez, R., Tabarini, D., Azpiazu, N., Frasch, M. & Schlessinger, J. The Drosophila insulin receptor homolog: a gene essential for embryonic development encodes two receptor isoforms with different signaling potential. *EMBO J.* **14**, 3373–3384 (1995).
21. Yenush, L. et al. The Drosophila insulin receptor activates multiple signaling pathways but requires insulin receptor substrate proteins for DNA synthesis. *Mol. Cell. Biol.* **16**, 2509–2517 (1996).
22. Choi, E. & Bai, X. C. The activation mechanism of the insulin receptor: a structural perspective. *Annu. Rev. Biochem* **92**, 247–272 (2023).
23. Li, J. et al. Synergistic activation of the insulin receptor via two distinct sites. *Nat. Struct. Mol. Biol.* https://doi.org/10.1038/s41594-022-00750-6 (2022).
24. Uchikawa, E., Choi, E., Shang, G., Yu, H. & Bai, X. C. Activation mechanism of the insulin receptor revealed by cryo-EM structure of the fully liganded receptor-ligand complex. *eLife* **8**, https://doi.org/10.7554/eLife.48630 (2019).
25. Li, J., Choi, E., Yu, H. & Bai, X. C. Structural basis of the activation of type 1 insulin-like growth factor receptor. *Nat. Commun.* **10**, 4567 (2019).
26. Gutmann, T. et al. Cryo-EM structure of the complete and ligand-saturated insulin receptor ectodomain. *J. Cell Biol.* **219**, https://doi.org/10.1083/jcb.201907210 (2020).
27. Scapin, G. et al. Structure of the insulin receptor-insulin complex by single-particle cryo-EM analysis. *Nature* **556**, 122–125 (2018).
28. Choi, E., Duan, C. & Bai, X. C. Regulation and function of insulin and insulin-like growth factor receptor signalling. *Nat. Rev. Mol. Cell Biol.* https://doi.org/10.1038/s41580-025-00826-3 (2025).
29. Li, J., Wu, J., Hall, C., Bai, X. C. & Choi, E. Molecular basis for the role of disulfide-linked alphaCTs in the activation of insulin-like growth factor 1 receptor and insulin receptor. *eLife* **11**, https://doi.org/10.7554/eLife.81286 (2022).
30. Tatar, M. Aging regulated through a stability model of insulin/insulin growth factor receptor function. *Front. Endocrinol.* **12**, 649880 (2021).
31. Liao, S. et al. Regulatory roles of Drosophila insulin-like peptide 1 (DILP1) in metabolism differ in pupal and adult stages. *Front. Endocrinol.* **11**, 180 (2020).
32. Post, S. et al. Drosophila insulin-like peptide dilp1 increases lifespan and glucagon-like Akh expression epistatic to dilp2. *Aging Cell* **18**, e12863 (2019).
33. Colombani, J., Andersen, D. S. & Leopold, P. Secreted peptide Dilp8 coordinates Drosophila tissue growth with developmental timing. *Science* **336**, 582–585 (2012).
34. Slaidina, M., Delanoue, R., Gronke, S., Partridge, L. & Leopold, P. A Drosophila insulin-like peptide promotes growth during nonfeeding states. *Dev. Cell* **17**, 874–884 (2009).
35. Brogiolo, W. et al. An evolutionarily conserved function of the Drosophila insulin receptor and insulin-like peptides in growth control. *Curr. Biol.* **11**, 213–221 (2001).
36. Post, S. et al. Drosophila insulin-like peptides DILP2 and DILP5 differentially stimulate cell signaling and glycogen phosphorylase to regulate longevity. *Front. Endocrinol.* **9**, 245 (2018).
37. Viola, C. M. et al. Structural conservation of insulin/IGF signalling axis at the insulin receptors level in Drosophila and humans. *Nat. Commun.* **14**, 6271 (2023).
38. Jumper, J. et al. Highly accurate protein structure prediction with AlphaFold. *Nature* **596**, 583–589 (2021).
39. Liu, Y., Liao, S., Veenstra, J. A. & Nassel, D. R. Drosophila insulin-like peptide 1 (DILP1) is transiently expressed during non-feeding stages and reproductive dormancy. *Sci. Rep.* **6**, 26620 (2016).
40. Tatar, M., Chien, S. A. & Priest, N. K. Negligible senescence during reproductive dormancy in Drosophila melanogaster. *Am. Nat.* **158**, 248–258 (2001).
41. Zheng, S. Q. et al. MotionCor2: anisotropic correction of beam-induced motion for improved cryo-electron microscopy. *Nat. Methods* **14**, 331–332 (2017).
42. Zhang, K. Gctf: Real-time CTF determination and correction. *J. Struct. Biol.* **193**, 1–12 (2016).
43. Zivanov, J. et al. New tools for automated high-resolution cryo-EM structure determination in RELION-3. *eLife* **7**, https://doi.org/10.7554/eLife.42166 (2018).
44. Meng, E. C. et al. UCSF ChimeraX: Tools for structure building and analysis. *Protein Sci.* **32**, e4792 (2023).
45. Emsley, P., Lohkamp, B., Scott, W. G. & Cowtan, K. Features and development of Coot. *Acta Crystallogr. D Biol. Crystallogr.* **66**, 486–501 (2010).
46. Liebschner, D. et al. Macromolecular structure determination using X-rays, neutrons and electrons: recent developments in Phenix. *Acta Crystallogr. D Struct. Biol.* **75**, 861–877 (2019).
47. Croll, T. I. ISOLDE: a physically realistic environment for model building into low-resolution electron-density maps. *Acta Crystallogr. D Struct. Biol.* **74**, 519–530 (2018).
48. Williams, C. J. et al. MolProbity: more and better reference data for improved all-atom structure validation. *Protein Sci.* **27**, 293–315 (2018).
49. Lin, F. et al. Total solid-phase synthesis of biologically active Drosophila insulin-like peptide 2 (DILP2). *Aust. J. Chem.* **70**, 208–212 (2017).
50. An, W. et al. Activation of the insulin receptor by insulin-like growth factor 2. *Nat. Commun.* **15**, 2609 (2024).
51. Park, J. et al. Activation of the insulin receptor by an insulin mimetic peptide. *Nat. Commun.* **13**, 5594 (2022).
52. Choi, E., Zhang, X., Xing, C. & Yu, H. Mitotic checkpoint regulators control insulin signaling and metabolic homeostasis. *Cell* **166**, 567–581 (2016).

Acknowledgements

Cryo-EM data were collected at the University of Texas Southwestern Medical Center (UTSW) Cryo-Electron Microscopy Facility, funded in part by the Cancer Prevention and Research Institute of Texas (CPRIT) Core Facility Support Award RP170644. The authors thank Dr. Stoddard for facility access. A portion of this research was supported by NIH grant U24GM129547 and performed at the PNCC at OHSU and accessed through EMSL (grid.436923.9), a DOE Office of Science User Facility sponsored by the Office of Biological and Environmental Research. The authors thank Marzia Miletto at PNCC for data collection. This work is supported in part by grants from the National Institutes Health (R01AG082801 and R37AG024360 to M.T.; R35GM142937 and R01DK132361 to E.C.; R35GM156386 to X.-C.B.), Columbia Diabetes Center (P30DK063608 to E.C.), Columbia Digestive and Liver Diseases Research Center (1P30DK132710 to E.C.), the Welch foundation (I-1944 to X.-C.B.), the Irma T. Hirschl award (to E.C.), and NHMRC of Australia Idea grant (APP2020781 to J.W.). The authors thank Feng Lin for the peptide synthesis. X.-C.B. is Virginia Murchison Linthicum Scholar in Medical Research at UTSW.

Author contributions

M.T., E.C., and X.-C.B. designed and supervised research. K.C., M.N., R.Y., M.H., C.H., and J.W. performed research and analyzed data. K.C., X.-C.B., E.C., M.T., and J.W. wrote the manuscript with input from all authors. All authors contributed to the editing and reviewing of the manuscript.

Competing interests

The authors declare no competing interests.

Additional information

Supplementary information The online version contains supplementary material available at https://doi.org/10.1038/s41467-025-64586-6.

Correspondence and requests for materials should be addressed to Marc Tatar, Eunhee Choi or Xiao-chen Bai.

Peer review information *Nature Communications* thanks the anonymous reviewer(s) for their contribution to the peer review of this work. A peer review file is available.

Reprints and permissions information is available at http://www.nature.com/reprints

Publisher's note Springer Nature remains neutral with regard to jurisdictional claims in published maps and institutional affiliations.

Open Access This article is licensed under a Creative Commons Attribution-NonCommercial-NoDerivatives 4.0 International License, which permits any non-commercial use, sharing, distribution and reproduction in any medium or format, as long as you give appropriate credit to the original author(s) and the source, provide a link to the Creative Commons licence, and indicate if you modified the licensed material. You do not have permission under this licence to share adapted material derived from this article or parts of it. The images or other third party material in this article are included in the article's Creative Commons licence, unless indicated otherwise in a credit line to the material. If material is not included in the article's Creative Commons licence and your intended use is not permitted by statutory regulation or exceeds the permitted use, you will need to obtain permission directly from the copyright holder. To view a copy of this licence, visit http://creativecommons.org/licenses/by-nc-nd/4.0/.

© The Author(s) 2025